Journal of Alloys and Compounds 1020 (2025) 179304

Contents lists available at ScienceDirect

Journal of Alloys and Compounds

journal homepage: www.elsevier.com/locate/jalcom

Interfacial engineering of MoS_2 and bimetallic MOF hybrid for superior piezo-photocatalytic hydrogen production and wastewater treatment

Daniel Masekela [a,*], Tunde L. Yusuf [b], Sheriff A. Balogun [a], Edwin Makhado [a], Omolara I. Adeniran [c], Kwena D. Modibane [a,d,**]

[a] Department of Chemistry, School of Physical and Mineral Sciences, University of Limpopo, Sovenga, Polokwane 0727, South Africa
[b] Department of Chemistry, Faculty of Natural and Agricultural Sciences, University of Pretoria, Private Bag X20, Hatfield, Pretoria 0028, South Africa
[c] School of Chemistry and Physics, University of KwaZulu-Natal, Westville Campus, Chiltern Hills, Private Bag X54001, Durban 4000, South Africa
[d] DSI-NRF SARChI Chair in Photoelectrocatalytic Hydrogen Production, Department of Chemistry, School of Physical and Mineral Sciences, University of Limpopo (Turfloop), Polokwane, Sovenga 0727, South Africa

ARTICLE INFO

Keywords:
Photocatalysis
Piezocatalysis
Piezo-photocatalysis
Hydrogen production
Degradation

ABSTRACT

A novel hybrid heterojunction composite (MoS_2@Cu/Co-MOF) was fabricated via hydrothermal method for hydrogen production via water splitting and wastewater treatment. The as-prepared MoS_2@Cu/Co-MOF heterostructure was characterised using X-ray diffraction (XRD), Transmission electron microscopy (TEM), Field emission-scanning electron microscopy (FE-SEM), Brunauer–Emmett–Teller (BET), UV-Vis Diffuse Reflectance Spectroscopy (UV–vis DRS), Electrochemical impedance spectroscopy (EIS) and Chronoamperometry (CA). The FE-SEM and TEM confirmed the formation of a heterojunction composite since their images showed multi-stacked layers of MoS_2 nanosheets uniformly grown onto the octahedral shape of Cu/Co-MOF. Furthermore, the optical and piezo-electrochemical properties of the MoS_2@Cu/Co-MOF heterostructure were improved as confirmed by UV-DRS and CA. The internal piezoelectric field generated through ultrasonic vibration improved the separation of photogenerated charge carriers, thus enhancing photocatalytic performance. Under synergistic effect (combination of photocatalysis and piezocatalysis), MoS_2@Cu/Co-MOF heterojunction composite exhibited maximum hydrogen (H_2) production of 1308.028 μmol, which was greater than under individual processes including photocatalysis (832.381 μmol) and piezocatalysis (1010.749 μmol). Furthermore, the MoS_2@Cu/Co-MOF heterojunction composite achieved the highest degradation efficiency of 82 % under both light and ultrasonic irradiation. The plausible hydrogen production and degradation mechanism was proposed. This study offers valuable insights into the development of highly efficient and versatile heterostructure materials aimed at producing clean hydrogen energy and water.

1. Introduction

The production of clean hydrogen (H_2) is necessary for achieving a sustainable and low-carbon energy future, by providing a zero-emission energy source. Several traditional methods, such as steam reforming, partial oxidation, and autothermal steam reforming, have been employed in the past years to produce a large amount of H_2. However these methods are associated with the emission of greenhouse gases (GHGs) which have a negative impact on the environment [1–5]. On the other hand, photocatalytic hydrogen production via water splitting offers several advantages over traditional methods. This technology is based on (i) harnessing sunlight (solar energy) and splitting mainly water as a renewable resource, (ii) it is a safe technology that does not depend on fossil fuels, thus reliable for decarbonization and climate change mitigation, (iii) it operates at atmospheric temperature and pressure, therefore doesn't require any heat or pressure [6,7]. However, the fast recombination of the photogenerated charge carriers (electrons (e^-) and holes (h^+)) compromises the efficiency of the photocatalytic performance, thus restricting its practical application [8–10]. To date, several strategies, including doping, heterojunction formation, and morphological control, have been used to improve the photocatalytic performance [11,12]. But, there's still a need for effective separation of

* Corresponding author.
** Corresponding author at: Department of Chemistry, School of Physical and Mineral Sciences, University of Limpopo, Sovenga, Polokwane 0727, South Africa.
E-mail addresses: masekeladaniel@gmail.com, daniel.masekela@ul.ac.za (D. Masekela), kwena.modibane@ul.ac.za (K.D. Modibane).

https://doi.org/10.1016/j.jallcom.2025.179304
Received 1 January 2025; Received in revised form 10 February 2025; Accepted 19 February 2025
Available online 21 February 2025

charge carriers and transfer for overall better photocatalytic performance.

Recently, the piezoelectric effect has been shown as another effective strategy to inhibit the recombination of photogenerated charge carriers. The deformation of piezoelectric materials under the influence of mechanical vibration generated an internal piezoelectric field for the suppression of charge carriers [13,14]. Various lead-based piezoelectric materials, such as lead zirconate titanate (PZT) has widely employed due to their high piezoelectric coefficient (d_{33} ~ 500–600 pC/N,), polarizability, and conductivity [15]. For example, Xu *et al.*[16] have demonstrated that in the presence of ultrasonic vibration, $PbTiO_3$/g-C_3N_4 heterostructure exhibited excellent photocatalytic performance due to spontaneous polarization. However, the toxicity of lead (Pb), a key component in PZT, raises significant health and environmental concerns. Due to the toxicity concerns associated with Pb, there has been a significant push towards developing and using lead-free piezoelectric materials.

Molybdenum disulfide (MoS_2) has been utilized as lead-free based piezo-photocatalyst for several applications, including photocatalytic water splitting due to its excellent piezoelectric and optical properties [17,18]. Furthermore, its narrow band gap enables the absorption of visible light and the generation of electron-hole pairs when exposed to light. Therefore, these properties have made MoS_2 an ideal photocatalyst for various photocatalytic applications. Despite these strengths, setbacks such as lower surface area, limited photon capture, catalytic active sites, and faster kinetic mass transfer. Hence, additional modification is required to improve the surface area and dispersion of the photocatalyst material.

Metal-Organic Frameworks (MOFs) are porous crystalline materials composed of metal ions or clusters connected by organic ligands. This arrangement creates a framework characterized by a substantial surface area and high porosity. Their modular structure permits precise adjustment of their chemical and physical properties [19]. In this regard, the synergistic effect of MOF-based semiconductor composites offers a novel material with excellent properties such as higher surface area, porosity, and good chemical stability. For instance, ZnO coupled with HKUST-1 MOF was reported for photocatalytic elimination of organic pollutants [20]. The hybrid composite (ZnO@MOF) possessed excellent degradation efficiency under sunlight exposure. In another study, ZnO-based heterostructure consisting of HKUST-1 MOF also showed an exceptional visible-light H_2 evolution rate of 467.1 μmol h^{-1} g^{-1} [21].

In the quest for wastewater treatment, various technologies have been implemented to purify wastewater. These methods include adsorption [22,23], membrane filtration [24–26], ozonation [27–29], and reverse osmosis [30,31]. However, some of these approaches come with drawbacks such as high operational costs, complexity, incomplete removal of contaminants, and the production of toxic secondary sludge [9]. On the other hand, semiconductor-based photocatalysis is regarded as an ideal solution to these challenges due to its cost-effectiveness, efficiency, and eco-friendly nature, as it directly harnesses solar energy [32].

To the best of our knowledge, the piezo-photocatalytic hydrogen production and wastewater purification using MoS_2 catalyst coupled with bimetallic MOF (Co/Cu-MOF) has not been reported yet. Hence, we report a novel hydrothermally synthesized MoS_2@Co/Cu-MOF heterostructure composite for photocatalytic, piezocatalytic, and piezo-photocatalytic hydrogen production and degradation of organic pollutants. The developed piezo-photocatalyst composite (MoS_2@Co/Cu-MOF) was confirmed using XRD, FTIR, FE-SEM, TEM, TGA, and BET. The overall study shows that bimetallic MOF-based coupled with piezocatalyst can be employed in various photocatalytic applications, including hydrogen production and wastewater treatment, due to their improved properties.

2. Materials and methods

2.1. Materials

All reagents used for synthesis were of analytical grade such as cobalt nitrate hexahydrate ($Co(NO_3)_2{\cdot}6\ H_2O$), copper nitrate hexahydrate ($Cu(NO_3).3H_2O$), benzene-1,3,5-tricarboxylic acid (BTC) and *N, N*-Dimethylformamide (DMF) were purchased from Sigma Aldrich, South Africa. The commercial bulk molybdenum disulfide (MoS_2) employed for the formation of heterojunction with Cu/Co-MOF was also purchased from Sigma Aldrich, South Africa. All compounds and chemicals were used as received without additional purification. Ultrapure distilled water was employed during the entire study.

2.2. Piezo-photocatalyst synthesis

Hydrothermal method was employed to synthesise Cu/Co-MOF [33]. Here, about 2.85 mmol of benzene-1,3,5-tricarboxylic acid (BTC) was dissolved in a mixture of DMF, ethanol, and distilled water (H_2O) with a volume (v) ratio of 2;2;1, respectively. The solution mixture was stirred for 30 min at room temperature. Thereafter, an amount of 3 mmol of $Cu(NO_3)_2.3H_2O$ and 2 mmol of $Co(NO_3)_2{\cdot}6\ H_2O$ were added to the above solution mixture and further stirred for an additional 30 min. The homogenous mixture consisting of $Cu(NO_3)_2.3H_2O$, $Co(NO_3)_2{\cdot}6\ H_2O$, and BTC was transferred into a Teflon autoclave and heated at 120 ° C for 24 hrs in an oven. The Cu/Co-BTC (MOF) precipitates were filtered and washed with a mixture of ethanol and deionised water several times.

To develop MoS_2@Cu/Co-MOF heterojunction composite, the same above hydrothermal synthetic route for the preparation of Cu/Co-MOF was followed, except that a certain amount of MoS_2 was added with $Cu(NO_3)_2.3H_2O$ and $Co(NO_3)_2{\cdot}6\ H_2O$ into BTC solution.

2.3. Characterisation analysis

X-ray diffraction (XRD, Ultima IV-Rigaku) was employed for phase identification and to investigate the purity of the fabricated piezo-photocatalyst. The external morphology of the materials was investigated using Field emission-scanning electron microscopy (FE-SEM, Zeiss Crossbeam 540) coupled with Energy dispersive X-ray spectroscopy (EDS). For internal morphological analysis, Transmission electron microscopy (TEM, JEM-2100, Japan) was employed. Agilent Cary 600 Series Fourier transform infrared spectroscopy (FTIR) was employed to detect the functional groups within the fabricated materials. The surface area and thermal stability were determined using Brunauer-Emmett-Teller (BET, St 1 on NOVA 800) and Thermogravimetric analysis (TGA, PerkinElmer, Paris), respectively. The rate of electron and hole recombination was determined by measuring photoluminescence (PL) emission peaks using a Fluorescence spectrophotometer (F-186 2710, HITACHI) at 440 nm excitation. The ciprofloxacin (CIP) concentration and optical properties were investigated using UV–vis spectrophotometer (Agilent Technologies Cary 60 UV–vis). Electrochemical properties, including electrochemical impedance spectroscopy (EIS), piezo-electrochemical behavior, and transient photocurrent response (TPR) were examined with an Autolab potentiostat (PGSTAT204).

2.4. Piezo-photocatalytic hydrogen production and degradation experiment

Photocatalytic H_2 production was conducted in a closed reaction cell, and an amount of 100 mg piezo-photocatalyst was added into 50 mL solution of distilled water (H_2O). The solution mixture was purged with nitrogen gas (N_2) prior to piezo-photocatalytic water splitting. In this experiment, 150 W Osram lamp and ultrasonicator were employed as sources of light and vibration irradiation, respectively. A 50 mL gas syringe was used to collect the volume of H_2 and O_2 produced. By assuming both gases act as ideal gases, an ideal gas law was utilized to

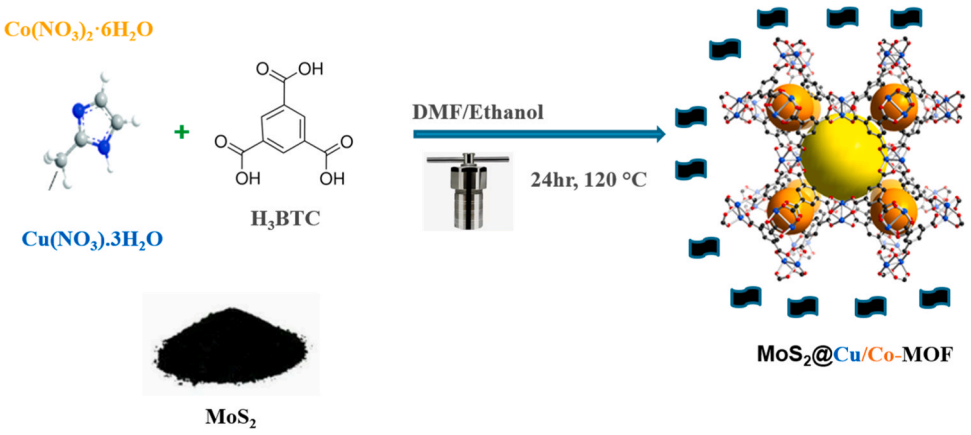

Scheme 1. Schematic representation for the preparation of MoS_2@Cu/Co-MOF heterojunction composite.

calculate the amount of H_2 and O_2 produced.

For the piezo-photocatalytic degradation of ciprofloxacin (CIP), a 100 W Xenon (Xe) lamp and UP400St ultrasonicator probe were used to initiate light irradiation and ultrasonic vibrations, respectively. In this process, 100 mg of the heterojunction composite was dispersed into 75 mL of a solution containing 5 ppm of CIP at neutral pH (6.5). The degradation of CIP was monitored at a wavelength of 276 nm using a UV–vis spectrophotometer (Agilent Technologies Cary 60 UV–vis) under simultaneous light irradiation and ultrasonic vibration. The solution was maintained at 25 ± 1°C using a circulating ice water bath. Aliquots of 4 mL were taken every 10 min throughout the degradation process.

3. Results and discussions

3.1. Structural analysis

Fig. 1**(a)** illustrates the FTIR spectra of Cu/Co-MOF and MoS_2@Cu/Co-MOF, which exhibit a peak at 731 cm^{-1} due to the coordination of metal ions (Cu^{2+}/ Co^{2+}) with O−C═O from the BTC organic linker [34]. The peaks at 1374 and 1445 cm^{-1} were assigned to the stretching of the aromatic ring. These stretching bands at the range of 1528–1610 cm^{-1} and 1373–1430 cm^{-1} correspond to the asymmetric and symmetric modes of the carboxylate groups in the Cu/Co-MOF. Similar vibration bands were observed in the MoS_2@Cu/Co-MOF composite spectrum; however, a slight difference was observed. The peak at 1715 cm^{-1} being characteristic of the partially coordinated benzene-1,3,5-tricarboxylic acid (BTC), became more distinct after the formation of heterostructure composite (MoS_2@Cu/Co-MOF). The FTIR spectra of MoS_2 shows a peak at 620 cm^{-1} corresponding to Mo–S stretching vibration [35], whereas other multiples peaks at lower bands (700–1150 cm^{-1}) can be attributed to sulfate groups and S-S bonds at 483 and 931 cm^{-1} [35] (Figure S1).

The XRD analysis was conducted to identify the phases and assess the purity of the fabricated piezo-photocatalyst [36]. As shown in Fig. 1**(b)**, the diffraction pattern of the MoS_2 nanosheets exhibited multiple peaks corresponding to the hexagonal structure (JCPDS no. 37–1492) [13,37]. Additionally, the presence of the (002) reflection with a d-spacing of 0.62 nm indicates that the MoS_2 nanosheets consist of multiple stacked layers, similar to bulk MoS_2 powder. The bimetallic MOF (Cu/Co-MOF) was highly crystalline, as observed in Fig. 1**(b)**. The fabricated bimetallic MOF displayed an XRD pattern similar to those of Cu-Co-BTC MOF reported in the literature [38]. The XRD pattern of the heterostructure composite (MoS_2@Cu/Co-MOF) showed a prominent (002) peak, confirming the successful formation of the heterostructure with Cu/Co-MOF. Both Cu/Co-MOF and MoS_2 peaks were present in the heterostructure composite (MoS_2@Cu/Co-MOF), with no additional peaks, indicating its high purity.

The external morphology of the prepared piezo-photocatalyst was examined using FE-SEM analysis at various magnifications. As depicted in Fig. 2**(a)**, the bimetallic MOF displayed a rough octahedral shape. At higher magnification, it is evident that this octahedral structure was formed by compacted nanorods (Fig. 2**(b)**). Fig. 2**(c,d)** shows multiple stacked layers of the fabricated MoS_2 nanosheets. The formation of the heterojunction is confirmed in Fig. 2**(e,f)**, where it can be clearly seen that the MoS_2 nanosheets are deposited on the surface of the octahedral bimetallic MOF. Additionally, the elemental analysis of the heterojunction composite revealed the presence of Mo from the MoS_2 and Cu/Co from the bimetallic MOF (Cu/Co-MOF), confirming the successful

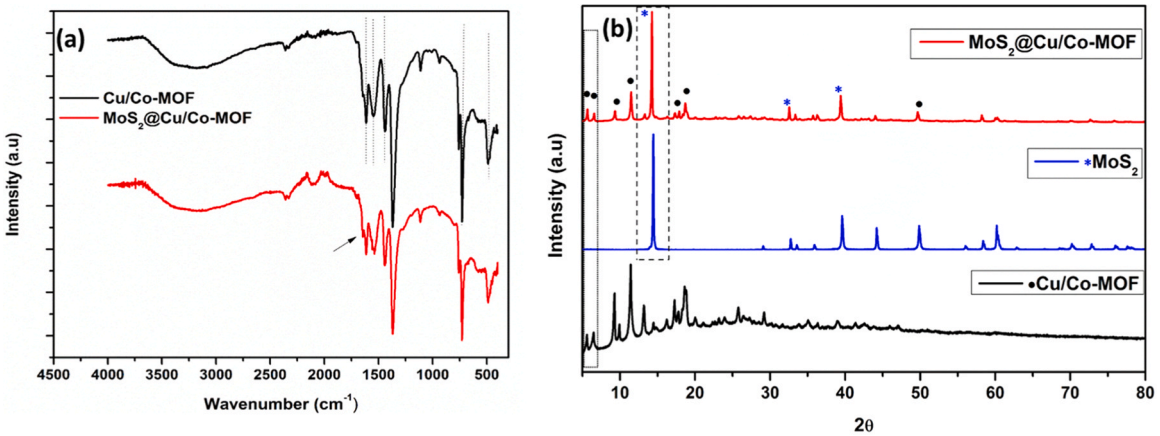

Fig. 1. (a) FTIR spectra and (b) XRD pattern of MoS_2, Cu/Co-MOF and MoS_2@Cu/Co-MOF.

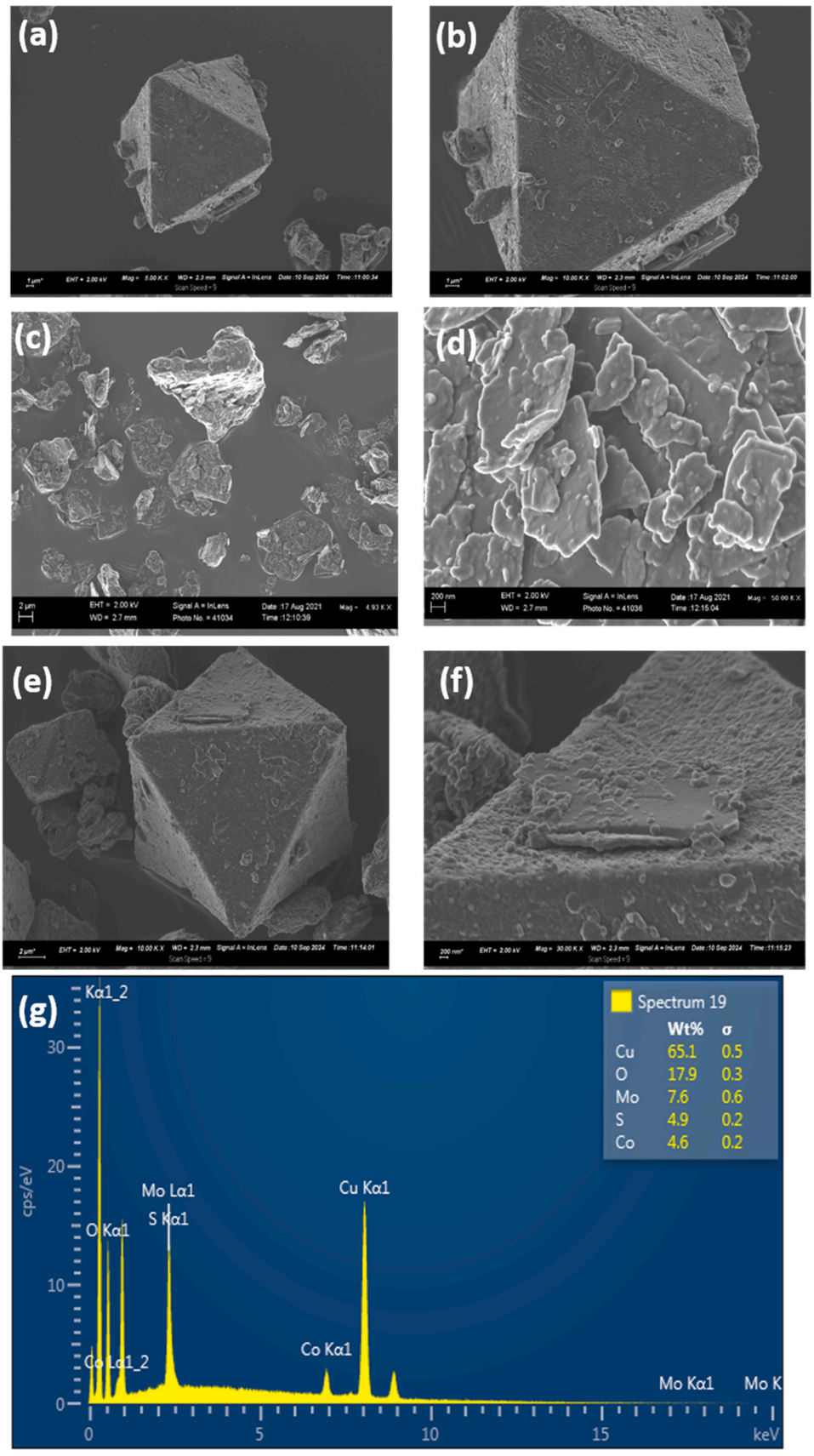

Fig. 2. FE-SEM images for (a,b) Cu/Co-MOF, (c,d) MoS_2, (e,f) MoS_2@Cu/Co-MOF at different magnifications and (g) EDS spectrum for heterojunction composite.

fabrication of the heterojunction composite (Fig. 2**(g)**).

The internal surface morphology of the developed piezo/photocatalyst materials was investigated using TEM at different magnifications (Fig. 3**(a-i)**). As depicted in Fig. 3 **(a-c)**, the bimetallic MOF exhibited a rod-like morphology structure. The small spherical particles on the surface of the nanorods demonstrate cobalt (Co) nanospheres. The 2D-MoS_2 showed an irregular multiple stacked sheets-like structure (Fig. 3**(d-f)**). The morphology of MoS_2@Cu/Co-MOF depicted in Fig. 3 **(g-i)** shows that the MoS_2 nanosheets were wrapped around the surface of Cu/Co-MOF. These TEM micrographs also provide more evidence for the successful formation of heterojunction composite (MoS_2@Cu/Co-MOF).

3.2. Thermal and surface analysis

Thermal Gravimetric Analysis (TGA) was employed to determine the thermal stability of the pristine materials and heterojunction composite. The bimetallic MOF (Cu/Co-MOF) exhibited three (3) distinctive decomposition steps (Fig. 4**(a)**). The first degradation step at around the temperature range of 28–100 °C is due to evaporation of the adsorbed water molecules on the surface, whereas as second degradation step which occurs at approximately 270–350 °C is attributed to the removal of solvent and water molecules which are trapped within the pores of the bimetallic MOF [39]. The last continuous thermal decomposition step around 400–600 °C is due to the disintegration of the BTC organic linker within the bimetallic MOF to form bimetallic oxide [40–44]. Upon successful formation of a heterojunction composite between MoS_2 and Cu/Co-MOF, it was noticed that the heterojunction composite also exhibited three distinctive decomposition steps similar to that of pristine Cu/Co-MOF. However, improved thermal stability was observed due to MoS_2 nanosheets wrapped around the surface of Cu/Co-MOF. This also confirms the successful formation of heterojunction composite.

The surface area and pore sizes of the developed piezo-photocatalyst materials play a significant role in piezo-photocatalytic process. As a result, the BET analyser was used to determine surface area of the porous materials fabricated. As shown from the nitrogen (N_2) sorption isotherms (Fig. 4**(b) and** Figure S2), the prepared materials (MoS_2, Cu/Co-MOF, and MoS_2@Cu/Co-MOF) showed type IV adsorption-desorption isotherms, suggesting their mesoporous structure according to International Union of Pure and Applied Chemistry (IUPAC) [45–47]. The BET surface area for MoS_2, Cu/Co-MOF, and MoS_2@Cu/Co-MOF were determined to be 5.295, 322.094, and 380.585 m^2/g, respectively (Table 1). It was observed that the heterojunction composite (MoS_2@Cu/Co-MOF) showed the highest specific surface area compared to pristine materials (MoS_2 and Cu/Co-MOF). This large surface area could provide more active sites within the heterojunction composite, which can improve the piezo/photocatalytic activity [48]. The average pore sizes were found to be 3.42, 3.84, and 3.40 nm for MoS_2, Cu/Co-MOF, and MoS_2@Cu/Co-MOF, respectively. This shows that the formation of heterojunction composite led to a slight decrease in pore size due to the possibility of MoS_2 being trapped within the porous structure of bimetallic MOF.

3.3. Optical and piezo-electrochemical properties

UV-Vis DRS analysis was employed to examine the wavelength regions at which the prepared piezo/photocatalyst absorbs photons. As shown in Fig. 5**(a)**, the optical properties were investigated at a wavelength range of 200–800 nm. All the samples absorbed the photons in the visible regions, Cu/Co-MOF and MoS_2@Cu/Co-MOF wavelength band-edges were extrapolated to be 433.568 and 473.706 nm, respectively. However, the MoS_2 nanosheets covered the whole absorption spectrum (200–800 nm). The formation of heterojunction between MoS_2 and Cu/Co-MOF extended the absorption wavelength edge of Cu/Co-MOF from 433.568 to 473.706 nm within MoS_2@Cu/Co-MOF, making heterojunction composite (MoS_2@Cu/Co-MOF) a better solar harvesting catalyst as compared to pristine materials.

The tauc's plots derived from the UV-DRS data were used to determine the direct band gaps of the materials by applying the Eq. (1.1) below:

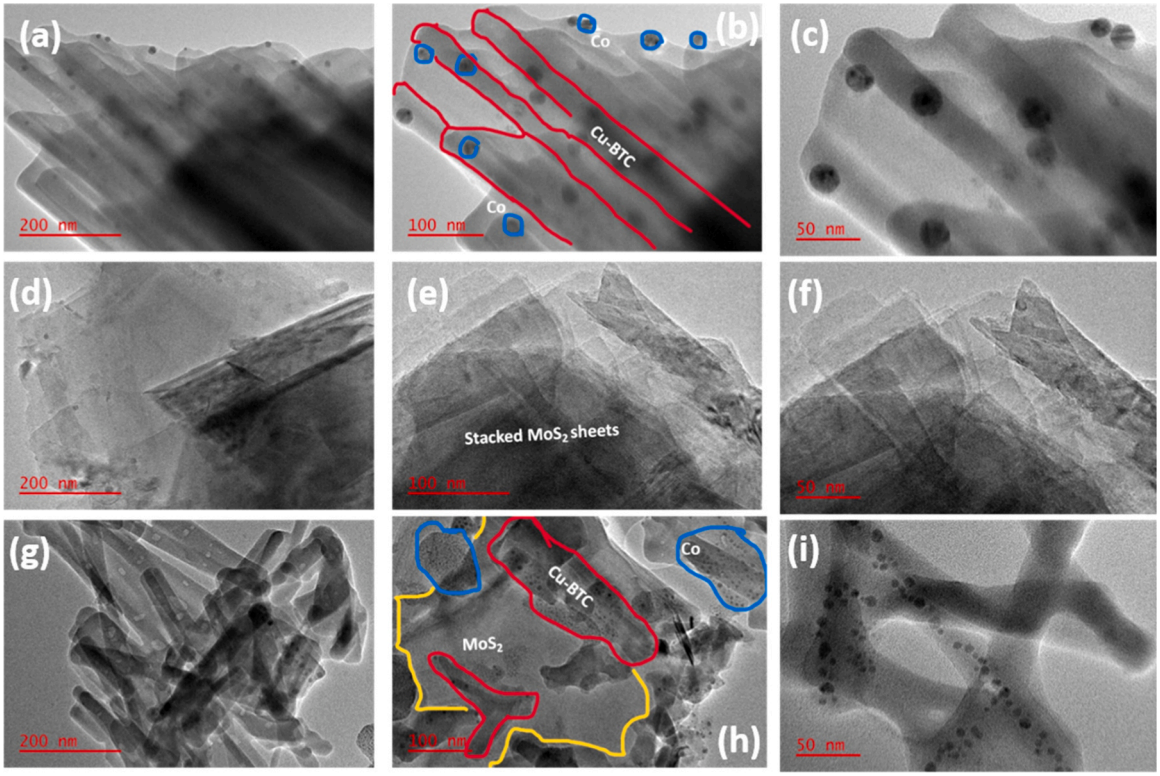

Fig. 3. TEM images for (a-c) Cu/Co-MOF, (d-f) MoS_2 and (g-i) MoS_2@Cu/Co-MOF at different magnifications.

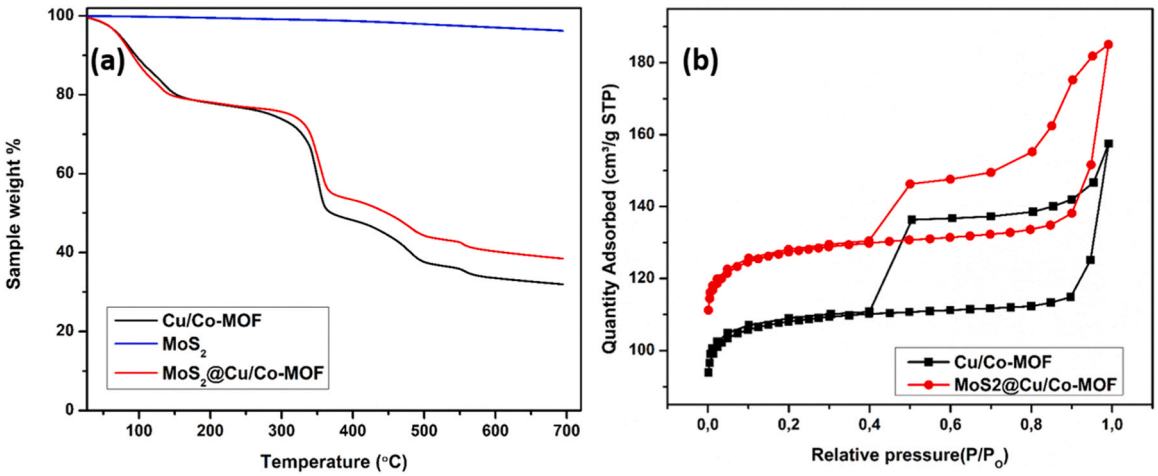

Fig. 4. (a) TGA and (b) BET analysis for MoS_2, Cu/Co-MOF and MoS_2@Cu/Co-MOF heterojunction composite.

Table 1
BET surface areas and pore sizes for MoS_2, Cu/Co/MOF and MoS_2@Cu/Co-MOF.

Catalyst	BET surface areas (m^2/g)	Pore sizes (nm)
MoS_2	5.295	3.42
Cu/Co-MOF	322.094	3.84
MoS_2@Cu/Co-MOF	380.585	3.40

$$(\alpha h\nu) = A(h\nu - Eg)^{n} \quad (1.1)$$

Where extinction coefficient, Planck's constant, incident light frequency, constant, and energy band gap are represented by α, *h*, *ν*, *A*, and E_g, respectively.

The extrapolated direct energy band gaps were found to be 2.86, 1.98 and 2.62 eV for Cu/Co-MOF, MoS_2 and MoS_2@Cu/Co-MOF, respectively. The formation of heterojunction between MoS_2 and Cu/Co-MOF improved charge carrier transfer and more efficient utilization of visible light, as demonstrated by UV-DRS spectra.

The Mott-Schottky (M-S) analysis was used to determine the flat band potential and the type of semiconductors employed. As shown from the M-S plot (Fig. 5**(e,f)**), the fabricated materials exhibited positive slopes, thus suggesting their n-type characteristics [49]. Based on the M-S plot, the extrapolated flat band potentials were obtained to be −0.78 and −0.63 (V vs Ag/AgCl), which is equivalent to −0.58 and −0.43 V vs normal hydrogen electrode (NHE) for MoS_2 and Cu/Co-MOF, respectively. The conduction band (CB) potential for n-type semiconductors is usually − 0.1 to −0.2 V more negative than the flat band potential [49,50], thus the corresponding CB/LUMO potentials were calculated to be −0.68, and −0.53 vs normal hydrogen electrode (NHE) for MoS_2 and Cu/Co-MOF, respectively. Furthermore, the obtained energy band gaps were used to determine valance band (VB) edge potentials using Eq. (1.2) below:

$$E_{VB} = E_g + \quad E_{CB} \quad (1.2)$$

According to the band gaps, the valence band (VB)/HOMO potentials were calculated to be 1.30 and 2.33 V vs NHE for MoS_2 and Cu/Co-MOF, respectively.

The photoluminescence (PL) was used to investigate the rate of the charge carrier recombination. From literature, it has been reported that lower PL intensity is associated with lower recombination rate of charge carriers [51,52]. The emission PL spectra showed that Cu/Co-MOF had highest PL intensity as compared to MoS_2 and MoS_2@Cu/Co-MOF (Fig. 6**(a)**). Therefore, suggesting that faster recombination of electrons and holes for Cu/Co-MOF. On the other hand, significant decrease in PL intensity was observed in MoS_2 nanosheets and the heterojunction composites. The MoS_2@Cu/Co-MOF heterojunction composite exhibited the lowest PL emission peak, with about 80 % reduction. This lower peak intensity demonstrates that the formation of heterojunction between MoS_2 and Cu/Co-MOF could inhibit or lower the rate of photogenerated electrons and hole recombination. Additionally, the low-energy tail of the PL spectrum suggests the presence of sub-bandgap features, likely due to defects in the MoS_2@Cu/Co-MOF heterojunction. The PL results indicate that MoS_2@Cu/Co-MOF excels in separating and transporting spatial electrons and holes, which is the main reason for its superior photocatalytic activity.

In addition, the transient photocurrent (TPC) response was conducted by switching visible light On/Off to determine the photoactivity of the fabricated piezo-photocatalyst in terms of their charge separation efficiency and the effective lifetime of charge carriers. As shown in Fig. 6 **(b)**, the heterojunction composite exhibited a higher photocurrent of 0.40 mA, which was 2.0 and 3.30 times greater than that of MoS_2 (0.2 mA) and Cu/Co-MOF (0.12 mA) pristine materials, respectively. These results further confirm that the formation of heterojunction between MoS_2 and Cu/Co-MOF could inhibit the fast recombination of photogenerated charge carriers, thus improving charge separation and transfer. Additionally, the high-intensity spike, referred to as decay, observed in the plot—unlike the simple rectangular "on-off" response—indicates that the photogenerated holes have a long lifetime. This also demonstrates significant band bending due to the accumulation of hole carriers near the photoanode interface, leading to electron depletion. The more pronounced the band bending, the better the charge separation, and the lower the recombination rate of photogenerated holes and electrons.

To determine the piezoelectric effect of the developed materials, chronoamperometry studies were conducted by switching ultrasonic vibration cycles On/Off. As observed in Fig. 6**(c)**, all samples have shown to exhibit a piezoelectric effect since, under ultrasonic vibration, a notable piezocurrent was generated. The MoS_2 nanosheets exhibited greater piezoelectrochemical current as compared to Cu/Co-MOF, because MoS_2 nanosheets as a piezoelectric material, have higher piezoelectric coefficients than MOFs. However, a significant increase in piezocurrent was observed when heterojunction formation between MoS_2 and Cu/Co-MOF was formed. This shows that coupling piezoelectric materials with MOFs could lead to generating an internal piezoelectric field under ultrasonic vibration, which can suppress the recombination of photogenerated electrons and holes, thus improving current mobility and separation of charge carriers. The piezoelectrochemical current exhibited by MoS_2 and Cu/Co-MOF and MoS_2@Cu/Co-MOF were 0.582, 0.467 and 0.838 mA, respectively (Table 2).

Furthermore, EIS was employed to investigate the charge migration

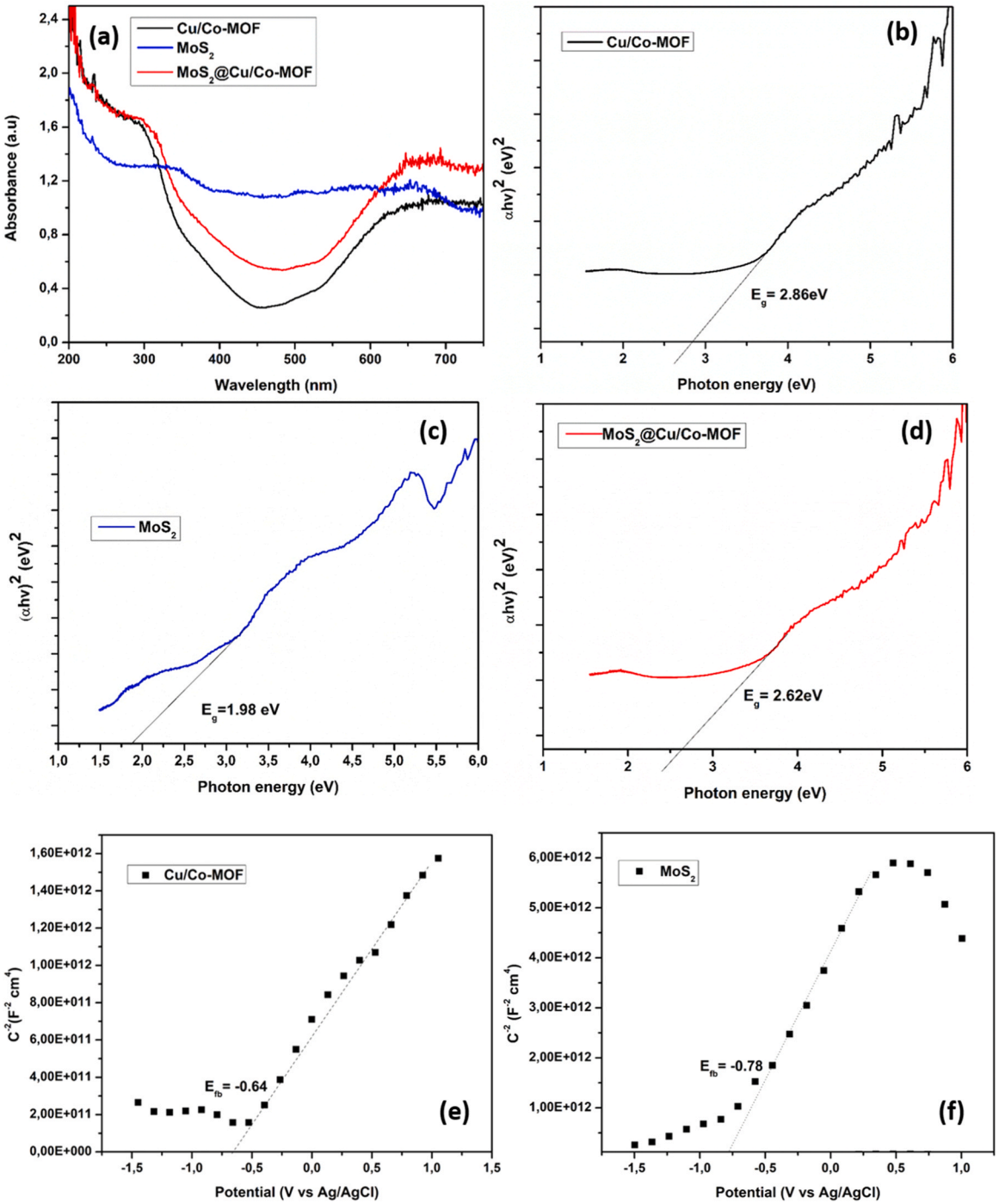

Fig. 5. (a) UV–vis DRS, (b,c) tauc's plots for MoS_2, Cu/Co-MOF and MoS_2@Cu/Co-MOF heterojunction composite and (e,f) M-S plot.

and separation of the piezo-photocatalyst. The semi-circular pattern shown in Fig. 6**(d)** results from the charge transfer process, with its resistance corresponding to the diameter of the semicircle. The pristine materials (MoS_2 and Cu/Co-MOF) had large semi-circles, suggesting higher charge transfer resistance (R_{ct}). The heterojunction formation led to a decrease in semi-circle, indicating its lowest interfacial charge transfer resistance (R_{ct}). This low charge transfer allows easy migration of electrons within the heterojunction composites, thus leading to suppression of photogenerated electrons and holes by improving photocatalytic activity. The R_{ct} values of the catalysts follow the order: MoS_2 > Cu/Co-MOF > MoS_2@Cu/Co-MOF. The heterojunction composite demonstrated improved charge separation compared to the pristine materials, as indicated by the photocurrent and piezocurrent response measurements in Fig. 6**(b,c)**).

3.4. *Piezo-photocatalytic hydrogen production*

The prepared piezo-photocatalyst (MoS_2, Cu/Co-MOF and MoS_2@Cu/Co-MOF) were investigated for photocatalytic, piezocatalytic and piezo-photocatalytic hydrogen production under different conditions (light irradiation, ultrasonic irradiation or both light and ultrasonic irradiation). Under light irradiation (photocatalysis), the pristine materials (MoS_2 and Cu/Co-MOF) exhibited low photocatalytic H_2 generation, which could be due to fast recombination of photogenerated charge carriers ((Fig. 7**(a,b)**). However, an improved photocatalytic H_2 generation was observed when a heterojunction composite (MoS_2@Cu/

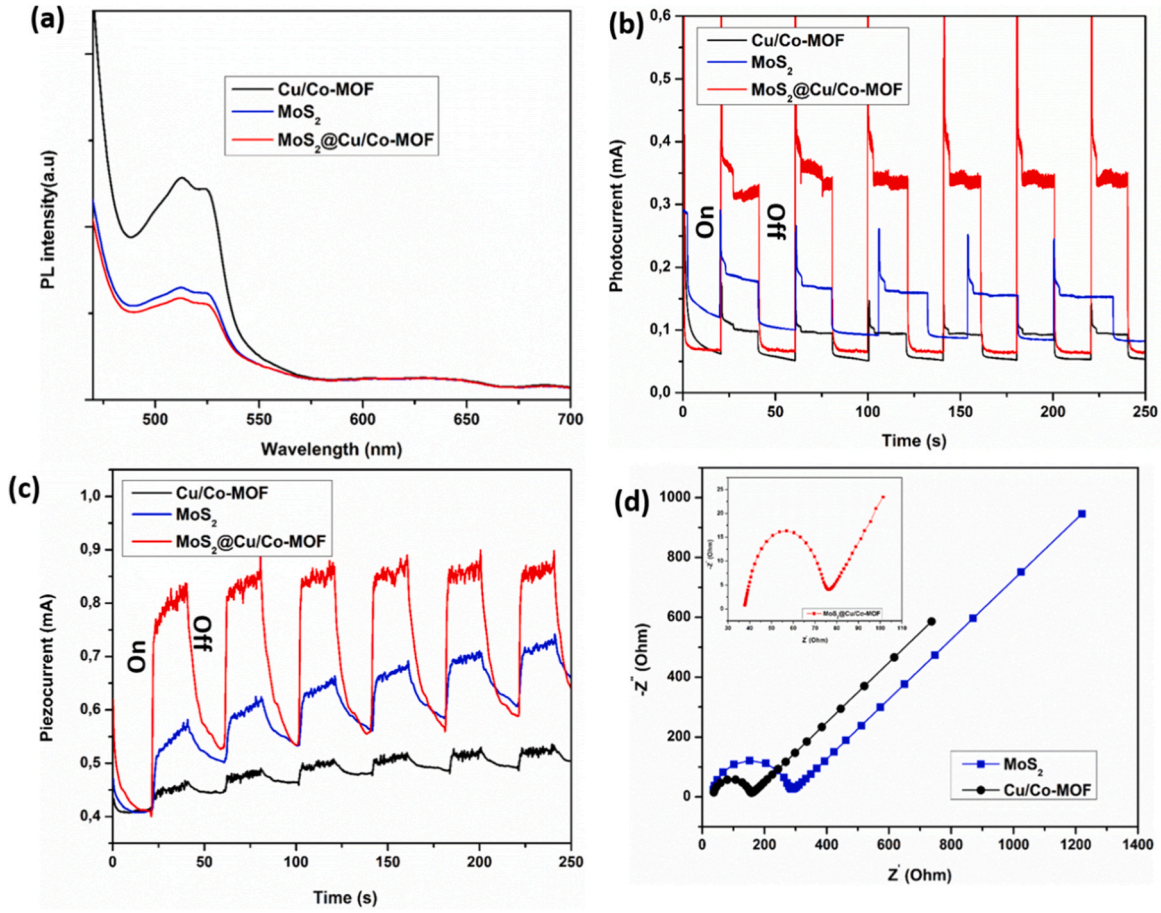

Fig. 6. (a) PL, (b) transient photocurrent response, (c) transient piezocurrent response and (d) EIS Nyquist plots for MoS_2, Cu/Co-MOF and MoS_2@Cu/Co-MOF heterojunction composites.

Table 2
Piezoelectrochemical and optical parameter measurements.

Catalyst	Photocurrent (mA)	Piezocurrent (mA)	Charge transfer resistance R_{ct} (Ω)	Energy band gap (eV)
MoS_2	0.20	0.582	292.44	1.98
Cu/Co-MOF	0.12	0.467	152.32	2.86
MoS_2@Cu/Co-MOF	0.40	0.838	76.49	2.62

Co-MOF) was employed. These results further confirm that the formation of a heterojunction composite between MoS_2 and Cu/Co-MOF could promote the separation of photogenerated carriers, thus improving photocatalytic performance. The amounts of H_2 generated were 401.327, 654.014, and 832.381 μmol using Cu/Co-MOF, MoS_2, and MoS_2@Cu/Co-MOF, respectively, after 30 min of light irradiation. Under ultrasonic vibration (piezocatalysis), MoS_2 demonstrated higher piezocatalytic H_2 production compared to Cu/Co-MOF (Fig. 7**(c,d)**). This is attributed to MoS_2's classification as a piezoelectric material with excellent piezoelectric properties. When the MoS_2 piezocatalyst undergoes mechanical vibration during ultrasonic irradiation, it generates a piezoelectric potential that drives free carriers to engage in redox reactions. Additionally, the formation of a heterojunction between MoS_2 and Cu/Co-MOF provides a large number of free carriers for the composite, thereby enhancing its piezocatalytic activity compared to the pristine MoS_2 sample. The MoS_2@Cu/Co-MOF heterojunction composite achieved the highest piezocatalytic H_2 production yield, approximately 1010.749 μmol, which was 1.6 and 4.8 times more than that of pure MoS_2 and Cu/Co-MOF, respectively. The piezo-photocatalytic H_2 production was investigated under both light and ultrasonic irradiation. As depicted in Fig. 7**(e,f),** the amount of H_2 generated by all piezo-photocatalysts during the piezo-photocatalytic process was significantly higher compared to either photocatalysis or piezocatalysis alone. This suggests that the synergy between ultrasonic vibration and light irradiation is crucial for enhancing hydrogen evolution. Piezo-photocatalytic H_2 produced was obtained at 1040.477 and 445.919 μmol for pure MoS_2 and Cu/Co-MOF, respectively. The exceptional piezo-photocatalytic H_2 generated by MoS_2@Cu/Co-MOF composite reached about 1308.028 μmol within 30 min. Comparing the H_2 production by heterojunction composite under different processes (photocatalysis, piezo-photo catalysis). It was observed that the H_2 production yield of the piezo-photocatalytic system was 1.3 times greater than that of the piezoelectric system and 1.6 times higher than that of the photocatalytic system. This further illustrates the synergistic effects of piezoelectric and photoelectrical mechanisms in the MoS_2@Cu/Co-MOF heterojunction composite. Our study was compared with other existing piezo-photocatalysts, as presented in Table S1. The synergistic effect was quantified using the Eq. (1.3) below:

$$Synergistic\ Effect = (HP_{combined} - HP_{expected})/HP_{expected} \quad (1.3)$$

Where $HP_{combined}$ is the hydrogen produced via piezo-photocatalysis, and $HP_{expected}$ is the sum of the hydrogen produced via photocatalysis and piezocatalysis.

A zero value indicates no synergy, whereas a positive and negative value indicates a positive and antagonistic effect, respectively. The calculated synergistic effect value was −0.29, thus confirming antagonistic effect synergy. This could be because, in a coupled system, the

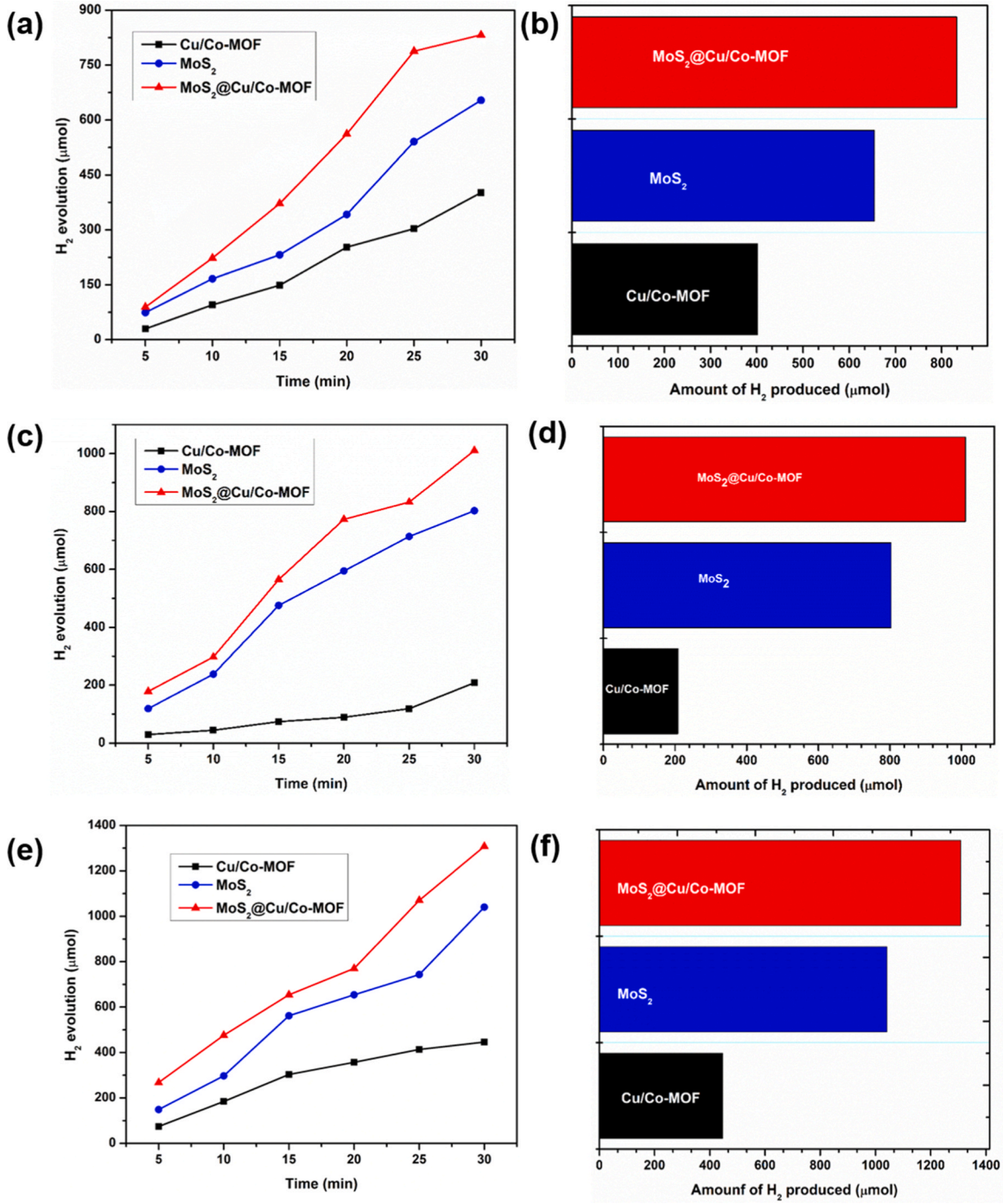

Fig. 7. (a,b) Photocatalytic (b,c) piezocatalytic and (c,d) piezo-photocatalytic hydrogen (H_2) production.

photocatalyst and piezocatalyst may compete for the same active sites on the material, reducing the overall efficiency of both processes. If the active sites are limited, the piezocatalytic and photocatalytic processes might hinder each other's effectiveness.

3.5. *Piezo-photocatalytic degradation*

The fabricated heterojunction composite was further analyzed for its ability to adsorb, as well as to degrade ciprofloxacin (CIP) through piezocatalytic and piezo-photocatalytic processes (Fig. 8**(a)**). During the adsorption process, without light or ultrasonic irradiation, the composite removed approximately 36 % of CIP from wastewater. When exposed to visible light, the MoS_2@Cu/Co-MOF achieved a maximum degradation efficiency of 60 % within 60 min. Notably, the introduction of mechanical force through ultrasonic vibration significantly enhanced the photocatalytic degradation. Under both light and ultrasonic irradiation, the degradation efficiency increased to 82 %. This improvement was attributed to the internal piezoelectric field generated by the piezocatalyst (MoS_2) under ultrasonic vibration, which reduced the rapid recombination of photogenerated electrons (e^-) and holes (h^+). The adsorption and degradation data were fitted using pseudo-first-order kinetics. The rate constants (k) were determined as the slope from the plot of $\ln(C_o/C_t)$ versus time (t) in Fig. 8**(b)**. From this plot, the derived rate constants (k) were 0.0060, 0.0142, and 0.0243 min^{-1} for adsorption, photocatalysis, and piezo-photocatalysis, respectively. These results demonstrate that the removal efficiency was significantly faster

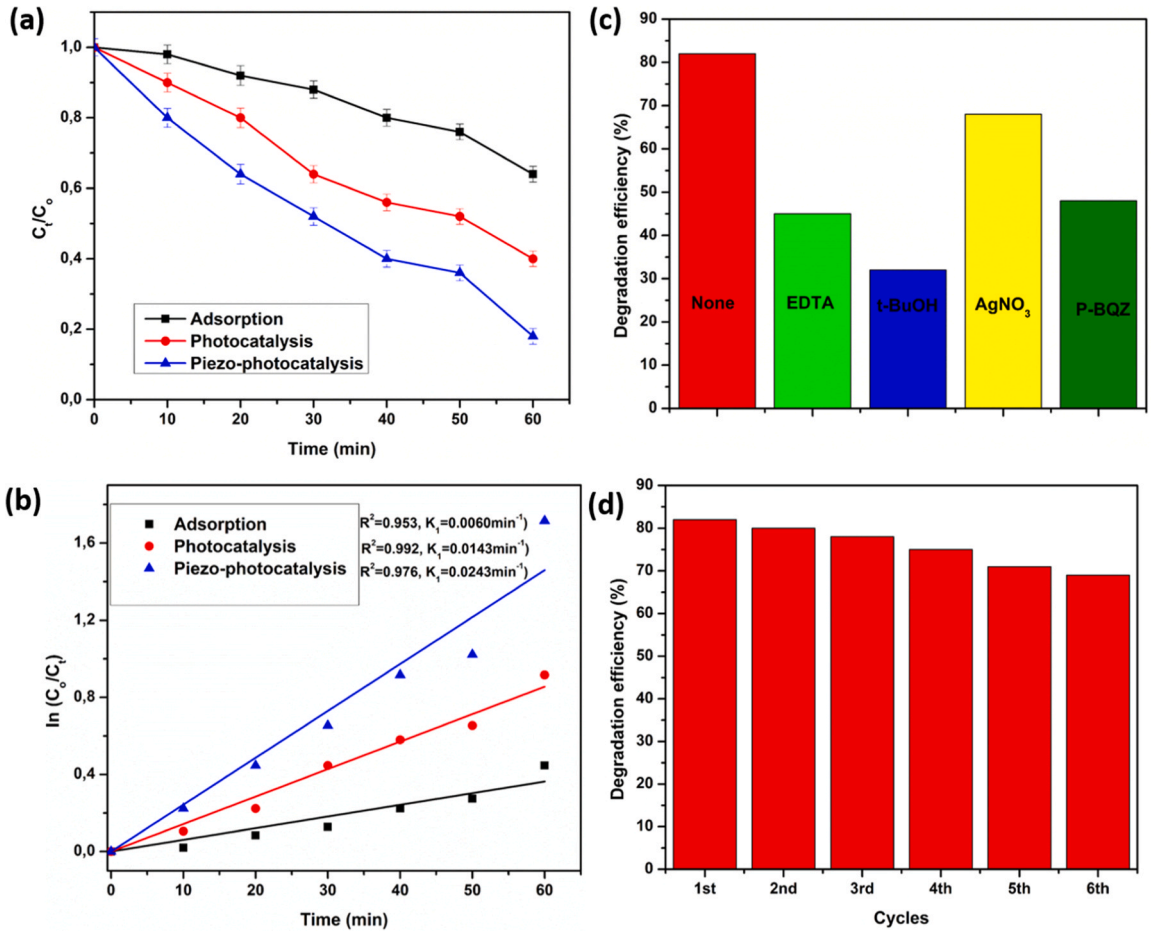

Fig. 8. (a) Piezo-photocatalytic degradation of CIP, (b) kinetic studies, (c) scavenger studies, and (d) cyclic experiment using heterojunction composite.

when piezo-photocatalysis was employed. Table S2 compares the findings of this study with those from existing literature.

To identify the active species responsible for the piezo-photocatalytic degradation of CIP, a trapping or scavenger experiment was conducted (Fig. 8**(c)**). In this experiment, tert-butanol (t-BuOH), ethylenediaminetetraacetate salt (EDTA), silver nitrate ($AgNO_3$), and p-benzoquinone (p-BZQ) were used as trapping agents to inhibit the generation of hydroxyl radicals (•OH), holes (h^+), electrons (e^-), and superoxide radicals ($\bullet O_2^-$), respectively. Without the trapping agents, the degradation efficiency was around 82 %. However, the addition of trapping agents led to a noticeable reduction in degradation efficiency. When t-BuOH was introduced, the efficiency dropped significantly from 82 % to 32 %, indicating that hydroxyl radicals ($^{\bullet}OH$) play a major role in the piezo-photocatalytic degradation of CIP. With the addition of EDTA and p-BZQ, the efficiency further decreased to 45 % and 48 %, respectively, suggesting that superoxide radicals ($^{\bullet}O_2^-$) and holes (h^+) are secondary active species. Electrons (e^-) had a minor role in the process, as the degradation efficiency remained relatively high (68 %) in the presence of $AgNO_3$.

The re-usability and stability of the MoS_2@Cu/Co-MOF heterojunction composite were investigated by performing a cyclic experiment. The cyclic experiment was carried out by using the same heterojunction composite for the degradation process for several cycles. After each cycle, the heterojunction composite was dried for 5 hrs in an oven at 60 °C. A noticeable reduction of 12 % degradation efficiency was observed after 6th cycle treatment (Fig. 8**(d)**), thus suggesting a possible reusability of the prepared heterojunction composite in real application.

3.6. *Proposed piezo-photocatalytic mechanisms*

Based on the band structure derived from the M-S plot, the calculated band positions can facilitate proton (H^+) reduction for H_2 generation and the formation of reactive oxygen species (ROS) such as hydroxyl radicals (•OH) and superoxide radicals ($\bullet O_2^-$) for the degradation of organic pollutants [49,53,54]. Scheme 2**(a)** (Type II band alignment) illustrates the piezo-photocatalytic mechanisms for the degradation of CIP. Under visible light irradiation, electrons (e^-) are excited from the valence bands of both MoS_2 and Cu/Co-MOF to their respective conduction bands, leaving behind holes (h^+). To prevent electron-hole recombination, electrons are transferred from the conduction band (CB) of MoS_2 to the LUMO of Cu/Co-MOF, as the CB potential of MoS_2 is higher than that of Cu/Co-MOF. These transferred electrons then react with oxygen (O_2), forming superoxide radicals ($\bullet O_2^-$), while the holes react with water (H_2O) to generate hydroxyl radicals (•OH). The resulting ROS are responsible for breaking down CIP into harmless by-products [55–57].

For piezo-photocatalytic H_2 production, a similar mechanism was proposed as shown in Scheme 2**(b)**. Similarly, both piezo-photocatalysts are subjected to visible light exposure, thus resulting in the excitation from the valance band to the conduction band, leaving the holes behind. Due to the higher CB potential of MoS_2, the electrons are migrated from the CB band of MoS_2 to the LUMO of Cu/Co-MOF, whereas holes from HOMO of Cu/Co-MOF accumulate in the VB of MoS_2 [49,58–60]. The migrated electrons in the CB of MoS_2 with strong reduction potential are used to catalyze the conversion of protons (H^+) to hydrogen gas (H_2) [49,61]. Additionally, ultrasonic vibrations generate a piezoelectric field at the interface, which serves as a driving force for the separation of

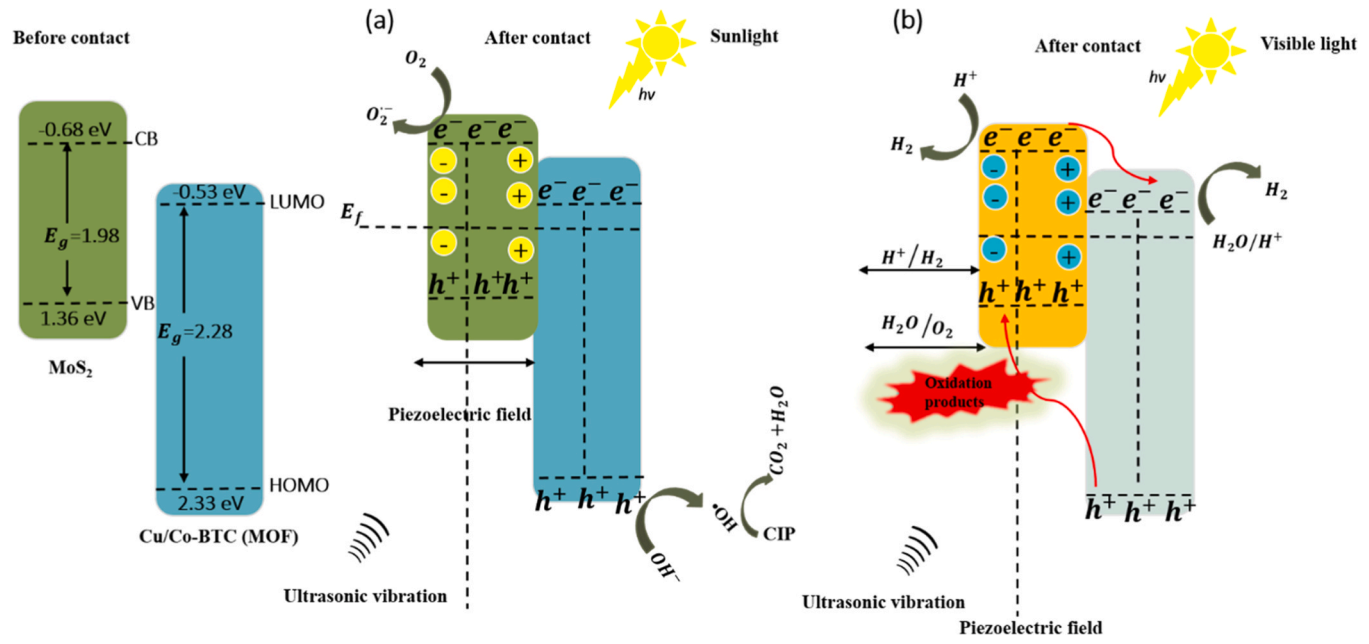

Scheme 2. Piezo-photocatalytic mechanism for (a) degradation of CIP and (b) hydrogen production.

electrons and holes, thereby enhancing the photocatalytic activity.

4. Conclusion

The formation of a heterojunction (MoS_2@Cu/Co-MOF) composite was successfully fabricated using the hydrothermal method. The fast recombination of electrons and holes was suppressed by the formation heterostructure composite and piezoelectric field. Additionally, poor charge carrier migration and visible-light capturing were improved via the formation of a heterojunction composite. The fabricated heterojunction composite was investigated for photocatalytic, piezocatalytic, and piezo-photocatalytic H_2 production and degradation of CIP. In comparison to piezocatalysis and photocatalysis, the piezo-photocatalytic activity of the heterojunction composite was greater. Under light and ultrasonic irradiation (piezo-photocatalysis), MoS_2@Cu/Co-MOF heterostructure produced approximately 1308.028 μmol of H_2 and exhibited a degradation efficiency of 82 %. Furthermore, combining photocatalysis and piezocatalysis processes improved H_2 production and degradation efficiency. This work provides new insights into the fabrication of heterostructure composite for various photocatalytic applications, including energy production and wastewater treatment.

CRediT authorship contribution statement

Yusuf Tunde Lewis: Writing – review & editing, Visualization, Validation. **Masekela Daniel:** Writing – original draft, Visualization, Validation, Methodology, Investigation, Formal analysis, Data curation, Conceptualization. **Balogun Sheriff Aweda:** Writing – review & editing, Visualization, Validation, Formal analysis. **Adeniran Omolara Ibikunoluwa:** Writing – review & editing. **Makhado Edwin:** Writing – review & editing, Methodology, Investigation. **Modibane Kwena Desmond:** Writing – review & editing, Resources, Project administration, Funding acquisition, Conceptualization.

Declaration of Competing Interest

The authors declare that they have no known competing financial interests or personal relationships that could have appeared to influence the work reported in this paper.

Acknowledgments

The authors would like to acknowledge the University of Limpopo, DSI/NRF SARChI Chair-150531 Grant No. RCGH22082353005, Competitive Support for Unrated Researchers (Grant No. SRUG2205035936), National Research Foundation (Thuthuka program-UIDs. 118113) for financial support.

Appendix A. Supporting information

Supplementary data associated with this article can be found in the online version at doi:10.1016/j.jallcom.2025.179304.

Data availability

No data was used for the research described in the article.

References

[1] S.A. Lee, J. Kim, K.C. Kwon, S.H. Park, H.W. Jang, Anion exchange membrane water electrolysis for sustainable large-scale hydrogen production, Carbon Neutralization 1 (2022) 26–48, https://doi.org/10.1002/cnl2.9.
[2] P. Nikolaidis, A. Poullikkas, A comparative overview of hydrogen production processes, Renew. Sustain. Energy Rev. 67 (2017) 597–611, https://doi.org/10.1016/j.rser.2016.09.044.
[3] R. Kothari, D. Buddhi, R.L. Sawhney, Comparison of environmental and economic aspects of various hydrogen production methods, Renew. Sustain. Energy Rev. 12 (2008) 553–563, https://doi.org/10.1016/j.rser.2006.07.012.
[4] H. Balat, E. Kirtay, Hydrogen from biomass - present scenario and future prospects, Int. J. Hydrog. Energy 35 (2010) 7416–7426, https://doi.org/10.1016/j.ijhydene.2010.04.137.
[5] H. Ishaq, I. Dincer, C. Crawford, A review on hydrogen production and utilization: challenges and opportunities, Int. J. Hydrog. Energy 47 (2022) 26238–26264, https://doi.org/10.1016/j.ijhydene.2021.11.149.
[6] K. Villa, J.R. Galán-Mascarós, N. López, E. Palomares, Photocatalytic water splitting: advantages and challenges, Sustain. Energy Fuels. 5 (2021) 4560–4569, https://doi.org/10.1039/d1se00808k.
[7] J. Zhu, M. Zäch, Nanostructured materials for photocatalytic hydrogen production, Curr. Opin. Colloid Interface Sci. 14 (2009) 260–269, https://doi.org/10.1016/j.cocis.2009.05.003.
[8] D. Masekela, N.C. Hintsho-Mbita, N. Mabuba, Application of a piezo-photocatalytic thin film (FTO/BaTiO3/SnO2) for enhanced degradation of organic pollutants and disinfection of wastewater, Ceram. Int. 49 (2023) 7566–7579, https://doi.org/10.1016/j.ceramint.2022.10.251.
[9] D. Masekela, N.C. Hintsho-Mbita, S. Sam, T.L. Yusuf, N. Mabuba, Application of BaTiO3-based catalysts for piezocatalytic, photocatalytic and piezo-photocatalytic degradation of organic pollutants and bacterial disinfection in wastewater: a

comprehensive review, Arab. J. Chem. 16 (2023) 104473, https://doi.org/10.1016/j.arabjc.2022.104473.
[10] T.L. Yusuf, B.O. Orimolade, D. Masekela, B. Mamba, N. Mabuba, The application of photoelectrocatalysis in the degradation of rhodamine B in aqueous solutions: a review, RSC Adv. 12 (2022) 26176–26191, https://doi.org/10.1039/d2ra04236c.
[11] B.O. Orimolade, A.O. Idris, U. Feleni, B. Mamba, Recent advances in degradation of pharmaceuticals using Bi2WO6 mediated photocatalysis – a comprehensive review, Environ. Pollut. 289 (2021) 117891, https://doi.org/10.1016/j.envpol.2021.117891.
[12] H. Fei, T. Zhao, W. Guo, X. Wang, J. Zhang, Z. Fei, Z. Feng, G. Liu, Strategies for enhancing activities of typical piezo-photocatalytic material and its applications in environmental remediation: a review, J. Environ. Chem. Eng. 12 (2024) 111650, https://doi.org/10.1016/j.jece.2023.111650.
[13] D. Masekela, N.C. Hintsho-Mbita, L.N. Dlamini, T.L. Yusuf, N. Mabuba, Internal piezoelectric field produced by tri-component (FTO: Sb-ZnO/MoS2) thin film for enhanced photocatalytic degradation of organic pollutants and antibacterial activity, Mater. Today Commun. 38 (2024) 108500, https://doi.org/10.1016/j.mtcomm.2024.108500.
[14] L. Jing, Y. Xu, M. Xie, Z. Li, C. Wu, H. Zhao, J. Wang, H. Wang, Y. Yan, N. Zhong, H. Li, J. Hu, Piezo-photocatalysts in the field of energy and environment: designs, applications, and prospects, Nano Energy 112 (2023) 108508, https://doi.org/10.1016/j.nanoen.2023.108508.
[15] Y. Pan, J. Song, K. Wang, Research progress and prospects of liquid-liquid triboelectric nanogenerators: mechanisms, applications, and future challenges, ACS Appl. Electron. Mater. (2024), https://doi.org/10.1021/acsaelm.4c01729.
[16] T. Xu, P. Niu, S. Wang, L. Li, High visible light photocatalytic activities obtained by integrating g-C3N4 with ferroelectric PbTiO3, J. Mater. Sci. Technol. 74 (2021) 128–135, https://doi.org/10.1016/j.jmst.2020.10.036.
[17] X. Li, Z. Ren, Q. Zhang, L. Guo, J. Wu, Y. Li, W. Liu, P. Li, Y. Fu, J. Ma, Piezo–photocatalytic reduction of toxic Cr(VI) ions based on MoS2 nanoflowers, Mater. Lett. 333 (2023) 133564, https://doi.org/10.1016/j.matlet.2022.133564.
[18] T. Ren, W. Tian, Q. Shen, Z. Yuan, D. Chen, N. Li, J. Lu, Enhanced piezocatalysis of polymorphic few-layered MoS2 nanosheets by phase engineering, Nano Energy 90 (2021) 106527, https://doi.org/10.1016/j.nanoen.2021.106527.
[19] S. Roy, J. Darabdhara, M. Ahmaruzzaman, ZnO-based Cu metal–organic framework (MOF) nanocomposite for boosting and tuning the photocatalytic degradation performance, Environ. Sci. Pollut. Res. 30 (2023) 95673–95691, https://doi.org/10.1007/s11356-023-29105-4.
[20] A.N. Ökte, D. Karamanis, E. Chalkia, D. Tuncel, The effect of ZnO or TiO2 loaded nanoparticles on the adsorption and photocatalytic performance of Cu-BTC and ZIF-8 MOFs, Mater. Chem. Phys. 187 (2017) 5–10, https://doi.org/10.1016/j.matchemphys.2016.11.059.
[21] Q. Li, Y. Wu, X. Ye, Y. Zeng, M. Ding, ZnO-based heterostructure constructed using HKUST-1 for enhanced visible-light photocatalytic hydrogen evolution, Appl. Catal. A Gen. 633 (2022) 118533, https://doi.org/10.1016/j.apcata.2022.118533.
[22] A. Khan Khanzada, H.E. Al-Hazmi, B. Śniatała, T. Muringayil Joseph, J. Majtacz, S. A.M. Abdulrahman, S.S. Albaseer, T.A. Kurniawan, Z. Rahimi-Ahar, S. Habibzadeh, J. Mąkinia, Hydrochar-nanoparticle integration for arsenic removal from wastewater: challenges, possible solutions, and future horizon, Environ. Res. 238 (2023), https://doi.org/10.1016/j.envres.2023.117164.
[23] D. Masekela, N.C. Hintsho-Mbita, N. Mabuba, Diethylamine functionalised Moringa oleifera leaves for the removal of chromium(VI) and bacteria from wastewater, Int. J. Environ. Anal. Chem. 00 (2020) 1–21, https://doi.org/10.1080/03067319.2020.1762873.
[24] F. Alavi, O.N. Ciftci, Purification and fractionation of bioactive peptides through membrane filtration: a critical and application review, Trends Food Sci. Technol. 131 (2023) 118–128, https://doi.org/10.1016/j.tifs.2022.11.024.
[25] Y. Gan, C. Ding, B. Xu, Z. Liu, S. Zhang, Y. Cui, B. Wu, W. Huang, X. Song, Antimony (Sb) pollution control by coagulation and membrane filtration in water/wastewater treatment: a comprehensive review, J. Hazard. Mater. 442 (2023) 130072, https://doi.org/10.1016/j.jhazmat.2022.130072.
[26] Y. Men, Z. Li, L. Zhu, X. Wang, S. Cheng, Y. Lyu, New insights into membrane fouling during direct membrane filtration of municipal wastewater and fouling control with mechanical strategies, Sci. Total Environ. 869 (2023) 161775, https://doi.org/10.1016/j.scitotenv.2023.161775.
[27] X. Li, L. Fu, F. Chen, S. Zhao, J. Zhu, C. Yin, Application of heterogeneous catalytic ozonation in wastewater treatment: an Overview, Catalysts 13 (2023), https://doi.org/10.3390/catal13020342.
[28] T. Ren, C. Ouyang, Z. Zhou, S. Chen, M. Yin, X. Huang, X. Zhang, Mn-doped carbon-Al2SiO5 fibers enable catalytic ozonation for wastewater treatment: Interface modulation and mass transfer enhancement, J. Hazard. Mater. 460 (2023) 132307, https://doi.org/10.1016/j.jhazmat.2023.132307.
[29] W. Lee, S. Choi, H. Kim, W. Lee, M. Lee, H. Son, C. Lee, M. Cho, Y. Lee, Efficiency of ozonation and O3/H2O2 as enhanced wastewater treatment processes for micropollutant abatement and disinfection with minimized byproduct formation, J. Hazard. Mater. 454 (2023) 131436, https://doi.org/10.1016/j.jhazmat.2023.131436.
[30] D. Patel, A. Mudgal, V. Patel, J. Patel, K. Park, P. Davies, N. Dhakal, Exergy analysis for enhanced performance of integrated batch reverse osmosis – Forward osmosis system for brackish water treatment, Desalination 580 (2024) 117548, https://doi.org/10.1016/j.desal.2024.117548.
[31] J. Minier-Matar, E. AlShamari, M. Raja, F. Khan, M. Al-Maas, A. Hussain, S. Adham, Detailed organic characterization of process water to evaluate reverse osmosis membrane fouling in industrial wastewater treatment, Desalination 572 (2024) 117128, https://doi.org/10.1016/j.desal.2023.117128.
[32] R.T. Hussain, M.S. Hossain, J.H. Shariffuddin, Green synthesis and photocatalytic insights: a review of zinc oxide nanoparticles in wastewater treatment, Mater. Today Sustain. 26 (2024) 100764, https://doi.org/10.1016/j.mtsust.2024.100764.
[33] F. Tian, C. Qiao, R. Zheng, Q. Ru, X. Sun, Y. Zhang, C. Meng, Synthesis of bimetallic-organic framework Cu/Co-BTC and the improved performance of thiophene adsorption, RSC Adv. 9 (2019) 15642–15647, https://doi.org/10.1039/c9ra02372k.
[34] Q. Zhao, L. Zhu, G. Lin, G. Chen, B. Liu, L. Zhang, T. Duan, J. Lei, Controllable synthesis of porous Cu-BTC@polymer composite beads for iodine capture, ACS Appl. Mater. Interfaces 11 (2019) 42635–42645, https://doi.org/10.1021/acsami.9b15421.
[35] G.A.M. Ali, M.R. Thalji, W.C. Soh, H. Algarni, K.F. Chong, One-step electrochemical synthesis of MoS2/graphene composite for supercapacitor application, J. Solid State Electrochem. 24 (2020) 25–34, https://doi.org/10.1007/s10008-019-04449-5.
[36] M. Akhtar, A. Khajuria, J.K. Sahu, J. Swaminathan, R. Kumar, R. Bedi, S.K. Albert, Phase transformations and numerical modelling in simulated HAZ of nanostructured P91B steel for high temperature applications, Appl. Nanosci. 8 (2018) 1669–1685, https://doi.org/10.1007/s13204-018-0854-1.
[37] Y. Liu, Y. Zhao, L. Jiao, J. Chen, A graphene-like MoS2/graphene nanocomposite as a highperformance anode for lithium ion batteries, J. Mater. Chem. A. 2 (2014) 13109–13115, https://doi.org/10.1039/c4ta01644k.
[38] F. Tian, C. Qiao, R. Zheng, Q. Ru, X. Sun, Y. Zhang, C. Meng, Synthesis of bimetallic – organic framework Cu / Co- BTC and the improved performance of thiophene, 47 (2019) 15642–15647. ⟨https://doi.org/10.1039/c9ra02372k⟩.
[39] A.M.P. Peedikakkal, I.H. Aljundi, Mixed-metal Cu-BTC metal-organic frameworks as a strong adsorbent for molecular hydrogen at low temperatures, ACS Omega 5 (2020) 28493–28499, https://doi.org/10.1021/acsomega.0c02810.
[40] K.E. Ramohlola, G.R. Monana, M.J. Hato, K.D. Modibane, K.M. Molapo, M. Masikini, S.B. Mduli, E.I. Iwuoha, Polyaniline-metal organic framework nanocomposite as an efficient electrocatalyst for hydrogen evolution reaction, Compos. Part B Eng. 137 (2018) 129–139, https://doi.org/10.1016/j.compositesb.2017.11.016.
[41] C. Chen, J. Li, Z. Tang, G. Liao, L. Nie, In-situ co-precipitation of Bi-MOF derivatives for highly sensitive electrochemical glucose sensing, Microchem. J. 199 (2024) 109897, https://doi.org/10.1016/j.microc.2024.109897.
[42] N. Singh, S. Dalakoti, H.N. Wamba, R. Chauhan, S. Divekar, S. Dasgupta, Aarti, Preparation of Cu-BTC MOF extrudates for CH4 separation from CH4/N2 gas mixture, Microporous Mesoporous Mater. 360 (2023) 112723, https://doi.org/10.1016/j.micromeso.2023.112723.
[43] S. Chuhadiya, R. Sharma, Himanshu, M.S. Dhaka, Concentration and LBL cycle evolution to the Cu-BTC metal organic framework: optimization as functional layer to the solar cell devices, Sol. Energy 253 (2023) 175–186, https://doi.org/10.1016/j.solener.2023.02.023.
[44] F. Raganati, V. Gargiulo, P. Ammendola, M. Alfe, R. Chirone, CO2 capture performance of HKUST-1 in a sound assisted fluidized bed, Chem. Eng. J. 239 (2014) 75–86, https://doi.org/10.1016/j.cej.2013.11.005.
[45] D. Masekela, N.C. Hintsho-Mbita, L.N. Dlamini, T.L. Yusuf, N. Mabuba, Internal piezoelectric field produced by tri-component (FTO: Sb-ZnO/MoS2) thin film for enhanced photocatalytic degradation of organic pollutants and antibacterial activity, Mater. Today Commun. 38 (2024) 108500, https://doi.org/10.1016/j.mtcomm.2024.108500.
[46] B.X. Zhou, Z.G. Zhou, G.F. Huang, D.N. Xiong, Q. Yan, W.Q. Huang, Q.L. Wang, Mass production of ZnxCd1-xS nanoparticles with enhanced visible light photocatalytic activity, Mater. Lett. 158 (2015) 432–435, https://doi.org/10.1016/j.matlet.2015.06.027.
[47] A.H. Shah, Z.U. Abideen, S. Maqsood, F. Rashid, R. Ullah, A.U. Rehman, M. Dildar, M. Ahmad, K. Ullah, M.N. Rafi, F. Teng, Porous Cu-based metal organic framework (Cu-MOF) for highly selective adsorption of organic pollutants, J. Solid State Chem. 322 (2023), https://doi.org/10.1016/j.jssc.2023.123935.
[48] A.S. Yusuff, L. Taofeek Popoola, E.I. Aderibigbe, Solar photocatalytic degradation of organic pollutants in textile industry wastewater by ZnO/pumice composite photocatalyst, J. Environ. Chem. Eng. 8 (2020), https://doi.org/10.1016/j.jece.2020.103907.
[49] X. Hao, J. Zhou, Z. Cui, Y. Wang, Y. Wang, Z. Zou, Zn-vacancy mediated electron-hole separation in ZnS/g-C3N4 heterojunction for efficient visible-light photocatalytic hydrogen production, Appl. Catal. B Environ. 229 (2018) 41–51, https://doi.org/10.1016/j.apcatb.2018.02.006.
[50] S.S. Yi, J.M. Yan, B.R. Wulan, S.J. Li, K.H. Liu, Q. Jiang, Noble-metal-free cobalt phosphide modified carbon nitride: an efficient photocatalyst for hydrogen generation, Appl. Catal. B Environ. 200 (2017) 477–483, https://doi.org/10.1016/j.apcatb.2016.07.046.
[51] X. Wang, Q. Li, L. Gan, X. Ji, F. Chen, X. Peng, R. Zhang, 3D macropore carbon-vacancy g-C3N4 constructed using polymethylmethacrylate spheres for enhanced photocatalytic H2 evolution and CO2 reduction, J. Energy Chem. 53 (2020) 139–146, https://doi.org/10.1016/j.jechem.2020.05.001.
[52] Z.J. Chen, H. Guo, H.Y. Liu, C.G. Niu, D.W. Huang, Y.Y. Yang, C. Liang, L. Li, J. C. Li, Construction of dual S-scheme Ag2CO3/Bi4O5I2/g-C3N4 heterostructure photocatalyst with enhanced visible-light photocatalytic degradation for tetracycline, Chem. Eng. J. 438 (2022), https://doi.org/10.1016/j.cej.2022.135471.
[53] P. Gotipamul, R. Maheswaran, S. Pandiaraj, S.A. Alqarni, S. Chidambaram, Piezo-photocatalytically enhanced H2 production and pollutant removal from ZnO nanorods grown on g-C3N4 layers, Mater. Today Sustain. 24 (2023) 100501, https://doi.org/10.1016/j.mtsust.2023.100501.

[54] J. Wang, G. Wang, B. Cheng, J. Yu, J. Fan, Sulfur-doped g-C3N4/TiO2 S-scheme heterojunction photocatalyst for Congo Red photodegradation, Chin. J. Catal. 42 (2020) 56–68, https://doi.org/10.1016/S1872-2067(20)63634-8.
[55] X. Liu, L. Xiao, Y. Zhang, H. Sun, Significantly enhanced piezo-photocatalytic capability in BaTiO3 nanowires for degrading organic dye, J. Mater. 6 (2020) 256–262, https://doi.org/10.1016/j.jmat.2020.03.004.
[56] T.L. Yusuf, O.C. Olatunde, D. Masekela, N. Mabuba, D.C. Onwudiwe, S. Makgato, Rational design of S–scheme Cd0.5Zn0.5S/CeO2 heterojunction for enhanced photooxidation of antibiotics and photoreduction of Cr(VI), Ceram. Int. (2024), https://doi.org/10.1016/j.ceramint.2024.08.397.
[57] T.L. Yusuf, O.C. Olatunde, D. Masekela, K.D. Modibane, D.C. Onwudiwe, S. Makgato, Charge redistribution in Nise2/Mos2 n–n heterojunction towards the photoelectrocatalytic degradation of ciprofloxacin, ChemElectroChem 11 (2024) 1–10, https://doi.org/10.1002/celc.202400309.
[58] Q. Huang, F. Zhu, F. Xiao, G. Zhang, H. Hou, J. Bi, S. Yan, H. Hao, Construction of the Z-scheme heterogeneous HKUST-1/BiVO4 nanorod composite for enhanced piezo-photocatalytic reduction performance of Cr(VI), Langmuir (2024), https://doi.org/10.1021/acs.langmuir.4c02834.
[59] D. Kumar, S. Sharma, N. Khare, Piezo-phototronic and plasmonic effect coupled Ag-NaNbO 3 nanocomposite for enhanced photocatalytic and photoelectrochemical water splitting activity, Renew. Energy 163 (2021) 1569–1579, https://doi.org/10.1016/j.renene.2020.09.132.
[60] S. Jia, Y. Su, B. Zhang, Z. Zhao, S. Li, Y. Zhang, P. Li, M. Xu, R. Ren, Few-layer MoS2 nanosheet-coated KNbO3 nanowire heterostructures: piezo-photocatalytic effect enhanced hydrogen production and organic pollutant degradation, (2019) 7690–7700. ⟨https://doi.org/10.1039/c9nr00246d⟩.
[61] T. Song, X. Zhang, P. Yang, Interface engineering of W2C/W2N co-catalyst on g-C3N4 nanosheets for boosted H2 evolution and 4-nitrophenol removal, Environ. Sci. Nano. (2022) 1888–1899, https://doi.org/10.1039/d2en00104g.